A Model of Strongly Forced Wind Waves

ALEXEY V. FEDOROV

Department of Geology and Geophysics, Yale University, New Haven, Connecticut

W. KENDALL MELVILLE

Scripps Institution of Oceanography, University of California, San Diego, La Jolla, California

ABSTRACT

A model of surface waves generated on deep water by strong winds is proposed. A two-layer approximation is adopted, in which a shallow turbulent layer overlies the lower, infinitely deep layer. The dynamics of the upper layer, which is directly exposed to the wind, are nonlinear and coupled to the linear dynamics in the deep fluid. The authors demonstrate that in such a system there exist steady wave solutions characterized by confined regions of wave breaking alternating with relatively long intervals where the wave profiles change monotonically. In the former regions the flow is decelerated; in the latter it is accelerated. The regions of breaking are akin to hydraulic jumps of finite width necessary to join the smooth "interior" flows and have periodic waves. In contrast to classical hydraulic jumps, the strongly forced waves lose both energy and momentum across the jumps. The flow in the upper layer is driven by the balance between the wind stress at the surface, the turbulent drag applied at the layer interface, and the wave drag induced at the layer interface by quasi-steady breaking waves. Propagating in the downwind direction, the strongly forced waves significantly modify the flow in both layers, lead to enhanced turbulence, and reduce the speed of the near-surface flow. According to this model, a large fraction of the work done by the surface wind stress on the ocean in high winds may go directly into wave breaking and surface turbulence.

1. Introduction

The preponderance of theories of surface waves are based on the idea of irrotational linear free waves, that is, waves propagating in an ideal fluid with no leading-order forcing acting on the body of the fluid and no departures from the classical free-surface boundary conditions. Such waves satisfy a linear dispersion relationship with gravity and surface tension as restoring forces. Departures from this idealized state are introduced as weak higher-order perturbations, including the effects of nonlinearity, wave growth due to the wind, and wave decay due to viscosity, turbulence, or weak (in the mean) intermittent breaking. The advantage of this approach is that it is anchored in the linear dispersion relationship with all the simplicity that it affords as a basis for perturbation expansions, and all the detailed understanding of the linear kinematics and dynamics. There is an extensive literature on surface waves that follows this approach and it has been the foundation of all extant wind wave theories and numerical wind wave prediction schemes (Komen et al. 1994). However, under strongly forced conditions in which the time scales for wave growth are comparable to, or not much greater than, the wave period, the dynamics of the waves may change significantly, and a new approach must be found.

Figure 1a (after Melville 1996) shows short, $O(0.1–1)$ m, waves at the ocean surface under winds in the range of 50–60 kt during a storm in the North Atlantic. From this angle it appears that the wave field is quasiperiodic with each wave breaking on the steep forward face, while the rear face is much less steep. Similar waves are to be found in the downwash of a helicopter hovering over a water surface. An example is shown in Fig. 1b, where it is seen that for sufficiently high radial velocities of the downwash, a quasiperiodic field of breaking waves is generated. Although such waves may differ in detail from the waves generated naturally by strong winds in the open ocean, one can still expect qualitative similarities. If such strongly forced wave

Corresponding author address: Alexey V. Fedorov, Dept. of Geology and Geophysics, Yale University, 210 Whitney Ave., P.O. Box 208109, New Haven, CT 06520.
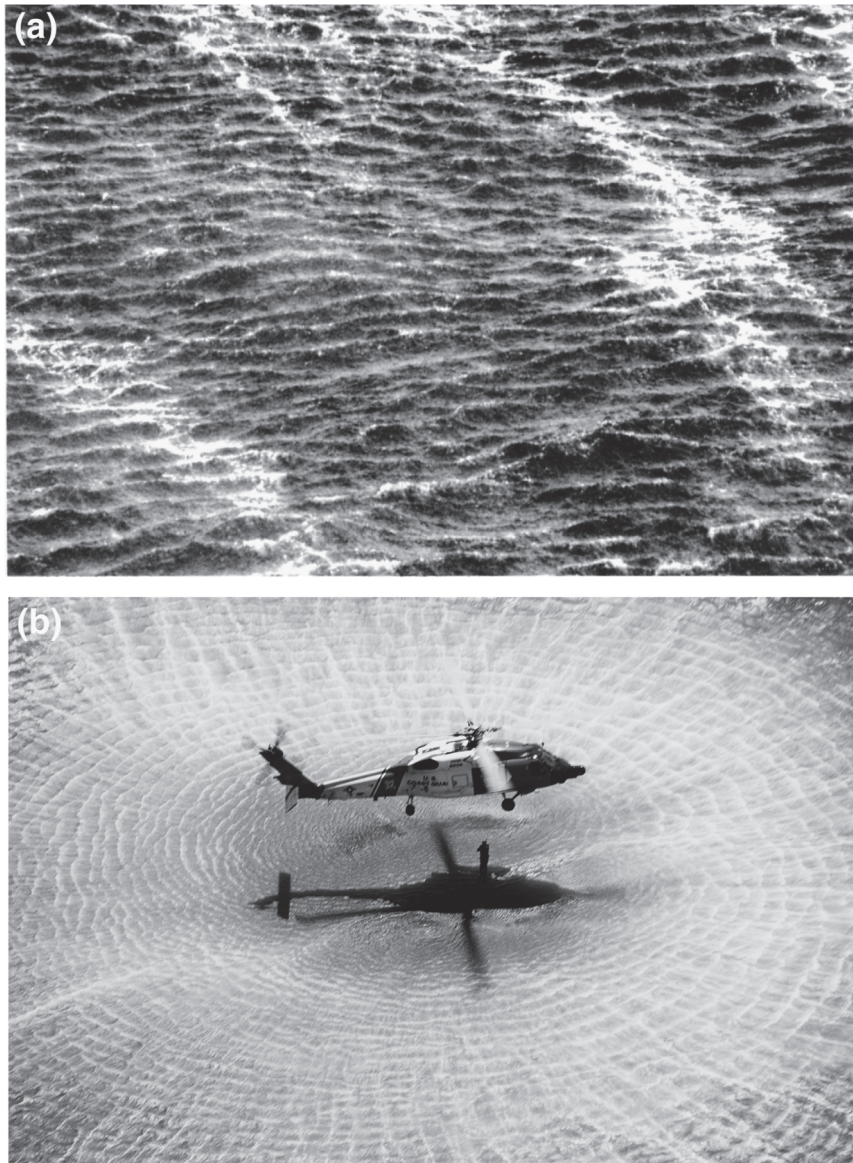E-mail: alexey.fedorov@yale.edu

FIG. 1. (a) Examples of relatively short, $O(0.1-1$ m$)$, strongly wind-forced breaking waves from a storm in the North Atlantic in December 1993 [After Melville (1996)]. (b) Breaking surface waves generated in the downwash of a helicopter hovering over a water surface (Photo courtesy of the U.S. Coast Guard).

fields could be described as approximately stationary and homogeneous, then to leading order the dissipation owing to the observed breaking and surface turbulence should balance the energy input from the wind.[1]

---

[1] Similar waves may be generated in very shallow water under strongly forced conditions in a shallow sound or estuary (with depths smaller than 1 m, say), where a well-mixed layer can be readily formed by the merging of the surface and bottom boundary layers. In that case, the depth of the water provides the vertical scaling for the long-wave dynamics, whereas in this paper the vertical scale is provided by the turbulent surface boundary layer.

Some observational and laboratory experimental results suggest that there is a qualitative change in air–sea interaction at high wind speeds. The drag coefficient of the ocean on the atmosphere, usually expressed as $C_D = (u_*/U_{10})^2$, where u_* is the friction velocity in the air and U_{10} is the wind speed at 10 m above the ocean surface, increases monotonically in the range 5–25 m s^{-1}. Recent evidence from airborne measurements of u_* in hurricanes (Powell et al. 2003) shows that, rather than continuing to increase, C_D reaches a maximum around 30 m s^{-1}, and may decrease slightly at higher wind

speeds. Recent laboratory measurements (Donelan et al. 2004) appear to be consistent with the field data; however, there is some uncertainty about scaling the laboratory results to the field. While there are many possible reasons for this regime change in air–sea interaction, a qualitative change in the wave field in high winds from one of intermittent breaking to one in which almost all the shorter waves are breaking is certainly plausible. Indeed, M. A. Donelan (2008, personal communication) has suggested that state in which almost all waves are breaking may decouple the aerodynamic drag of the boundary layer from the geometry of the surface through the effects of flow separation (Banner and Melville 1976) on the flow above. If almost continuous breaking is responsible, then models of strongly forced trains of breaking waves, like the one described in this paper, may be needed to better understand these processes.

In a study of steady gravity–capillary waves with a pressure forcing at the surface and viscous dissipation in the surface boundary layer, Fedorov and Melville (1998) found that under sufficiently strong forcing, and hence dissipation, strongly asymmetric solutions for the wave profile can be found with steep forward faces modulated by capillary waves and long upwind faces of smaller slope. The dissipation in these solutions is predominantly in the neighborhood of the capillary waves. In effect, the regions of high surface curvature associated with the capillary waves provide the dissipation that may in reality be afforded by the turbulence associated with breaking in naturally occurring strongly forced wave fields.

These observations and models lead us to consider quasiperiodic strongly wind-forced waves, including the effects of breaking-induced turbulence. The dynamics are similar in some respects to those of roll waves. Shallow flows down inclined planes (e.g., the spillway of a dam) are unstable, giving rise to roll waves. These have been modeled either as monotonic solutions joined by jump (shock) conditions to form periodic shallow water wave solutions, or by turbulent models in which eddy viscosity suppresses the jumps and leads to continuous periodic solutions with regions of large gradients corresponding to the jumps (Dressler 1949; Whitham 1974; Ng and Mei 1994; Balmforth and Mandre 2004). In the case of roll waves, the flow is driven by the balance between the component of gravity parallel to the plane and the stress at the bottom. For an extensive treatment of roll-wave models and the solutions of the model equations, see Balmforth and Mandre (2004). While motivational, the analogy between the roll waves and the strongly forced waves on deep water is relatively limited, as will become clear in the following sections.

In an open ocean, the "shallow" vertical scale is not so apparent as there is no solid boundary near the surface to support the hydrostatic pressure variations along the wave profile. Nevertheless, one can assume that breaking and near-surface turbulence are essential parts of the processes being modeled and lead to an enhanced (eddy) viscosity in a shallow layer near the surface. Thus, it is the layer of enhanced viscosity that defines the shallow layer that is strongly forced by the wind above and able to interact with the deep layer below. The dynamics of the upper layer are nonlinear and coupled to the dynamics of the deep fluid. The flow in the upper layer is controlled by the balance between the wind stress at the surface, the turbulent drag at the interface between the layers, and the wave drag induced at the interface by steadily breaking waves.

The idea that surface waves can be generated through the instability of a surface shear layer has a long tradition (Milinazzo and Saffman 1990; Morland et al. 1991; Shrira 1993; Longuet-Higgins 1998). Those authors assume that the wind creates a horizontal shear layer near the surface that rapidly becomes unstable to surface perturbations. In fact, Shrira (1993) showed that in a realistic parameter range the growth rates for such instability can be larger than those for the Miles's (1957, 1959) mechanism of surface wave generation. The approach of the present paper follows the idea of the presence of a surface layer, but here we assume it is turbulent, having already become unstable to shear. We assume that the momentum flux due to tangential wind stress leads to a formation of a shallow shear layer near the surface directly driven by the wind. This layer can become unstable very rapidly, generating short breaking waves and turbulence and thus creating the thin layer with enhanced eddy viscosity near the surface, which is necessary for our model.

We do not claim in this study that for all strongly forced wind regimes the air–sea momentum exchange takes place just through the wind shear stress at the sea surface, but rather that there exists a wave regime where this mechanism is a potentially important contributor.[2] How significant this mechanism is remains to be explored by laboratory and field studies.

The structure of the paper is as follows. In section 2 we formulate the problem, study the linear stability of the system, and introduce the "quasi nonlinear" approach, for which the dynamics are chosen to be nonlinear only in the upper layer. The numerical results are described in section 3 (the initial value problem),

---

[2] An extension of the model in appendix A designed to include form drag at the surface shows qualitatively similar results to the model with shear stress only.

section 4 (steady-wave solutions), and section 6 (the sensitivity of the results to changes in the main physical parameters of the problem). Important balances, including the energetics, are considered in section 5. Section 7 summarizes the main conclusions of the study. In appendix A we show how fluctuations in normal pressure induced by variations in the slope of the free surface can affect our solutions. Finally, appendix B illustrates the effects on the wave profiles of varying the viscosity in the upper layer.

2. Formulation of the problem

The approach adopted in this work can be easily understood from the sketch in Fig. 2, which shows a shallow (turbulent) layer resting on top of the lower, infinitely deep layer. The undisturbed thickness of the upper layer is δ. We will require that $k\delta \ll 1$, where $k = 2\pi/\lambda$ is the wavenumber and λ is the wavelength of the surface waves. This permits us to use the long-wave approximation for the motion in the upper layer. The flow in the lower layer is assumed to be irrotational; however, the dissipative effects of viscosity are incorporated by a standard modification of the boundary conditions at the interface between the two layers.

The waves are treated as two-dimensional in space, with x and z as the horizontal and vertical coordinates, and t as time. For the upper layer, τ denotes a uniform wind stress applied to the surface, $h(x, t)$ the total local upper-layer depth, $\zeta(x, t)$ the elevation of the free surface, and $U(x, t)$ the horizontal component of the velocity, independent of z in the long-wave approximation. In the lower layer $u(x, z, t)$ and $w(x, z, t)$ denote the horizontal and vertical velocity components, respectively; $\phi(x, z, t)$ is the velocity potential; and $\eta(x, t)$ is the displacement of the interface between the two layers; $P(x, z, t)$ and P_a are the pressures in the water and in the atmosphere, respectively; g is the acceleration of gravity, and ρ is the density of the water. Variables x, z, and t used in subscripts denote the corresponding derivatives.

The equations of motion in the upper layer are

$$(Uh)_t + (U^2 h)_x + gh\zeta_x = \tau/\rho - \gamma U^2 + \nu(hU_x)_x, \quad (1)$$

$$h_t + (Uh)_x = 0, \quad (2)$$

where

$$\zeta = h + \eta - \delta. \quad (3)$$

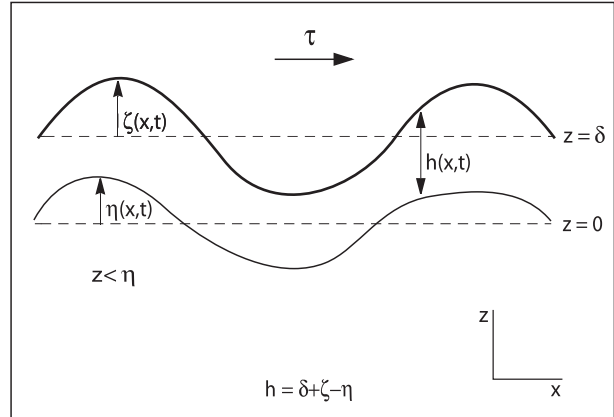The pressure field $P(x, z, t)$ is assumed to be hydrostatic in the upper layer; that is,

FIG. 2. Sketch of the two-layer fluid with the upper turbulent layer riding on an infinitely deep layer.

$$P = P_a + \rho g(\delta + \zeta - z). \quad (4)$$

In appendix A we consider how adding a simple modification to the pressure field proportional to the surface slope (which allows for a form drag) affects the solutions. Equations (1) and (2) describe the momentum and mass balance in the upper layer in the long-wave approximation. The term $\nu(hU_x)_x$ is a conventional turbulent momentum transport term in which ν is the turbulent (or eddy) viscosity (e.g., Gent 1993; Balmforth and Mandre 2004). We use constant values of ν for most of the calculations, but demonstrate in the appendix B that making viscosity a function of the horizontal gradient in the thickness of upper layer, and hence increasing viscosity in the regions of breaking, affect our solutions very little. The turbulent stress at the interface between the lower and upper layers is parameterized by quadratic damping ($-\gamma U^2$), with γ a constant.

The flow in the lower layer $-\infty < z \leq \eta$ is irrotational, satisfying Laplace's equation:

$$\phi_{xx} + \phi_{zz} = 0, \quad (5)$$

where

$$(u, w) = (\phi_x, \phi_z). \quad (6)$$

At $z = \eta$,

$$\eta_t + u\eta_x = w + 2\mu\eta_{xx}, \quad (7)$$

and

$$\phi_t + \frac{u^2}{2} + \frac{w^2}{2} + \frac{P - P_a}{\rho} + g\eta = g\delta + 2\mu\phi_{xx}, \quad (8)$$

where

$$P = P_a + \rho g(\delta + \zeta - \eta). \qquad (9)$$

The equations of motion for the lower layer are similar to the conventional description of irrotational surface waves generated by a pressure forcing. For example, the potential of the flow ϕ defined in (6) goes to zero at great depth:

$$\phi \to 0 \quad \text{as} \quad z \to -\infty. \qquad (10)$$

Equation (7) is the kinematic boundary condition, and Eqs. (8) and (9) provide the dynamic boundary condition for irrotational flows. In principle, we permit a discontinuity in the tangential component of the velocity at the interface between the layers, but require the continuity of the normal velocity and normal pressure.

An important note on modeling turbulent viscosity in the lower layer is necessary. Although viscous effects in the lower layer are not modeled directly, two additional terms describing viscous dissipation are added to the rhs of (7) and (8). These terms are chosen to describe two principle mechanisms contributing to dissipation: the direct effect of friction (the dissipative term in the dynamic boundary condition) and the effect of a viscous boundary layer near the interface. Longuet-Higgins (1992) and Ruvinsky et al. (1991) discussed these effects in application to free-surface flows. Similar viscous terms were used in the dynamic and kinematic boundary conditions for free-surface flows by Dommermuth (1994), Fedorov and Melville (1998), and others. Here, these additional terms are chosen to give classical viscous dissipation in the absence of the upper layer and in the limit of linear surface waves, with an amplitude decay rate of $2\mu k^2$. Values of the eddy viscosity, μ, much larger than molecular viscosity are used to account for turbulence generated by wave breaking. Thus, even though the motion in the lower layer remains irrotational [according to Eq. (6)], the dissipative effects due to turbulence are included in the model. Ultimately, these terms in the kinematic and dynamic boundary conditions are necessary for simulating breaking regions with a finite width.

Substituting (9) into (8) yields the final form of the dynamic boundary condition at $z = \eta$:

$$\phi_t + \frac{u^2}{2} + \frac{w^2}{2} + g\eta = 2\mu\phi_{xx}. \qquad (11)$$

To ensure the validity of the hydrostatic approximation we require that

$$\frac{\lambda}{\delta} \gg 1. \qquad (12)$$

The hydrostatic approximation also requires that vertical accelerations are small compared to gravity. Using incompressibility to scale w as $U_c\delta/\lambda$, where U_c is a characteristic velocity in the upper layer ($U_c = c_o$, or U_o), we require that

$$\frac{U_o^2\delta}{\lambda^2} \ll g; \quad \frac{c_o^2\delta}{\lambda^2} \ll g, \qquad (13)$$

where $c_o = \sqrt{g/|k|}$, $k = 2\pi/\lambda$ and U_o is the characteristic velocity of the wind-driven current in the upper layer (in the absence of the waves). Combining (12) and (13) gives

$$\lambda \gg \delta \max(1, U_o/c_s, c_o/c_s), \qquad (14)$$

where $c_s = \sqrt{g\delta}$. This condition (14) holds well in the parameter range of interest.

a. The linear approximation

While solving the complete system of equations, (1)–(11), is a difficult undertaking, and a matter of ongoing work, there are several approximate procedures that can help elucidate the most important properties of the solutions. The first is a conventional linearization with respect to the mean state, followed by a stability analysis.

The zeroth-order solution for this system is given by

$$U^2 = \frac{\tau}{\rho\gamma}, \qquad (15)$$

$$h = \delta, \qquad (16)$$

$$\zeta = 0, \qquad (17)$$

$$\eta = 0, \qquad (18)$$

$$\phi = 0, \qquad (19)$$

and

$$(u, w) = 0, \qquad (20)$$

which corresponds to a wind-driven upper layer with the uniform velocity U_o. There is no motion in the lower layer in the zeroth-order approximation. The balance in the upper layer is between the surface wind stress and friction at the interface between the layers. Using this solution as the basic state, introducing $\xi = \zeta - \eta$ instead of η, and linearizing (1)–(11) yields the following equations:

the linearized equations of motion for the upper layer

$$U_t + U_o U_x + g\zeta_x = -\frac{2\gamma U_o}{\delta}U + \nu U_{xx}, \qquad (21)$$

$$\xi_t + U_o\xi_x + \delta U_x = 0, \qquad (22)$$

and the linearized equations of motion for the lower layer

$$\phi_{xx} + \phi_{zz} = 0 \quad \text{for} \quad -\infty < z \le 0 \qquad (23)$$

with

$$\zeta_t - 2\mu\zeta_{xx} = \phi_z + \xi_t - 2\mu\xi_{xx} \quad \text{and} \qquad (24)$$

$$\phi_t + g\zeta = 2\mu\phi_{xx} \qquad (25)$$

at $z = 0$.

To study the stability of the system to small wavelike perturbations, we adopt the standard procedure and set

$$(U, \xi, \zeta) = \text{Re}[(\tilde{U}, \tilde{\xi}, \tilde{\zeta}) \exp i(kx - \omega t)]. \qquad (26)$$

The potential that satisfies the Laplace equation and decays at larger depths is

$$\phi = \text{Re}[\tilde{\phi} \exp(|k|z + ikx - i\omega t)]. \qquad (27)$$

Substituting (26) and (27) into the linearized set yields relationships between the complex amplitudes $\tilde{U}, \tilde{\xi}, \tilde{\zeta}$, and $\tilde{\phi}$:

$$i(kU_o - \omega)\tilde{U} + igk\tilde{\zeta} = -\frac{2\gamma U_o}{\delta}\tilde{U} + \nu(ik)^2\tilde{U}, \qquad (28)$$

$$i(kU_o - \omega)\tilde{\xi} + i\delta k\tilde{U} = 0, \qquad (29)$$

$$-i\omega\tilde{\zeta} - 2\mu(ik)^2\tilde{\zeta} = |k|\tilde{\phi} - i\omega\tilde{\xi} - 2\mu(ik)^2\tilde{\xi}, \qquad (30)$$

and

$$-i\omega\tilde{\phi} + g\tilde{\zeta} = 2\mu(ik)^2\tilde{\phi}. \qquad (31)$$

The eigenvalues of this system are given by the condition

$$\det\mathbf{A} = 0, \qquad (32)$$

where

$$\mathbf{A} = \begin{bmatrix} ikU_o - i\omega + \dfrac{2\gamma U_o}{\delta} - \nu(ik)^2 & 0 & igk & 0 \\ i\delta k & ikU_o - i\omega & 0 & 0 \\ 0 & i\omega + 2\mu(ik)^2 & -i\omega - 2\mu(ik)^2 & -|k| \\ 0 & 0 & g & -i\omega - 2\mu(ik)^2 \end{bmatrix}. \qquad (33)$$

First, let us assume that dissipation is negligible by setting $\gamma = \mu = \nu = 0$. Then (32) and (33) yield a simple dispersion relation for the linear waves:

$$(\omega^2 - g|k|)(\omega - U_o k)^2 = \omega^2 k^2 g\delta. \qquad (34)$$

After introducing $c = \omega/k$, $c_o = \sqrt{g/k}$ and $c_s = \sqrt{g\delta}$, Eq. (34) can be rewritten as

$$(c^2 - c_o^2)(c - U_o)^2 = c_s^2 c^2 = k\delta c_o^2 c^2. \qquad (35)$$

Equation (35) has a simple physical interpretation. If $k\delta \ll 1$, there are two types of waves in the system: surface gravity waves (two branches), and waves of advection (also two branches), modified by the interaction term on the rhs of (35). For very short waves, there are two branches of gravity waves in the neighborhood of $c = 0$ and two branches of kinematic waves (Whitham 1974, p. 26) in the neighborhood of $c = U_o$. As the wavelength increases (k decreases), one gravity wave branch merges with an advective branch to give a pair of complex conjugate roots and, hence, instability. Figure 3 shows a typical example of the wave phase speed and, for the unstable solutions, the growth rates, obtained by

solving Eq. (35). Introduction of dissipation terms reduces the growth rates and shifts the wavelengths of the most unstable waves toward longer wavelengths.

Figure 4 shows the growth rates, the wavelengths, and the phase speeds of the most unstable waves as a function of δ and U_o for the full system: Eqs. (32) and (33). The lengths of the waves may vary from tens of centimeters to several meters. Significantly, the phase speed of the most unstable waves is always slower than the speed of the current. The wave growth rates given by the model are quite high, but one can expect weaker growth rates for more realistic (continuous rather than stepwise) shear near the surface, which avoid surfaces of infinite vorticity.

b. The "quasi nonlinear" approximation: Formulation and numerical approach

The linear approach of the previous section predicts that the system will become unstable to small perturbations but cannot describe the eventual evolution of the disturbances. The next step, which can answer whether steady finite-amplitude wave solutions are possible, is to incorporate nonlinearity. Here, we will assume that
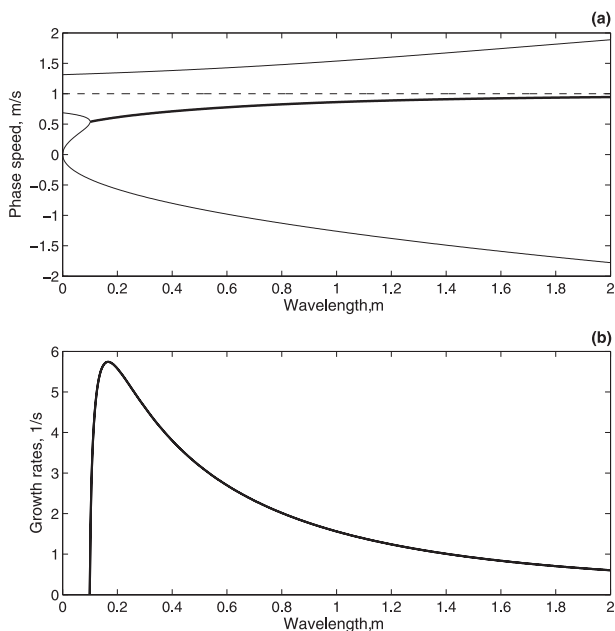
FIG. 3. (a) The linear phase speed as a function of the wavelength λ for four different branches of the solutions of Eq. (35). When two branches merge (the heavy line), the waves become unstable. The calculations were conducted for $\delta = 1$ cm and $U_o = 1$ m s^{-1}. The dashed line shows the value of U_o. (b) The exponential growth rate as a function of wavelength for the unstable branches.

nonlinearity is important only in the upper layer, while the fluid motion in the deep layer can still be considered linear. Although the validity of such an approximation is somewhat limited, this approach greatly simplifies the overall treatment of the problem, while providing some insight into the effects of nonlinearity.

First, let us rewrite the linearized equations (24) and (25), assuming that the mean flow in the lower layer is nonzero:

$$\eta_t + U_d \eta_x = \phi_z + 2\mu \eta_{xx} \tag{36}$$

and

$$\phi_t + U_d \phi_x + g\zeta = 2\mu \phi_{xx}, \tag{37}$$

at $z = 0$.

Here we have introduced U_d, a drift velocity in the lower layer induced by the tangential stress across the lower boundary of the upper layer. The transfer of momentum across the interface requires such a drift velocity, and we parameterize it as a linear function of U_o:

$$U_d = \alpha U_o, \tag{38}$$

where α is a parameter between 0 and 1. While this is a crude approximation, it is consistent with the phenom-
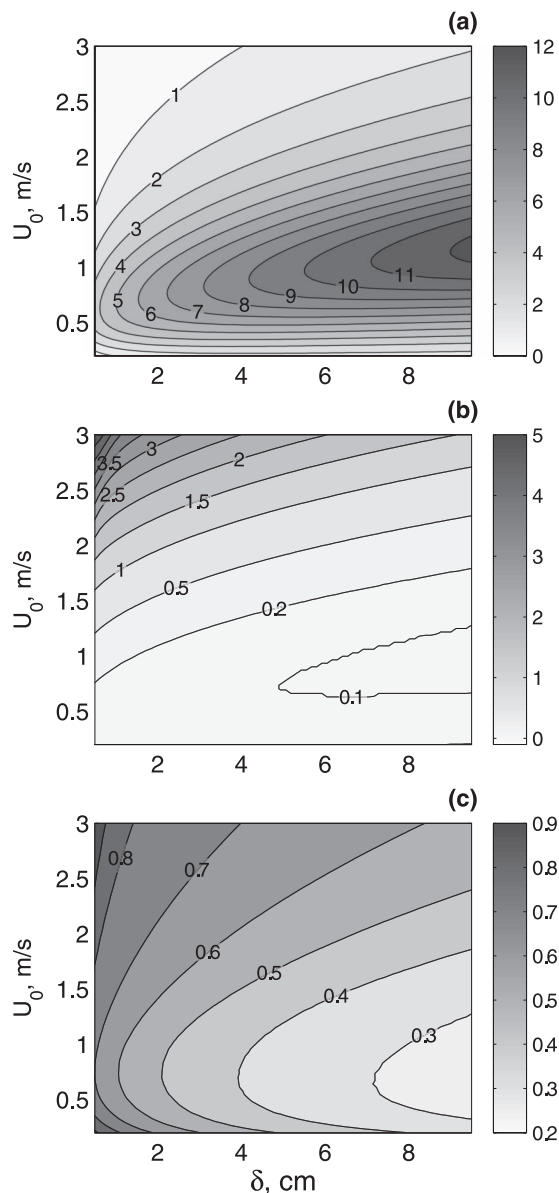

FIG. 4. The (a) exponential growth rates (s^{-1}), (b) wavelength (m), and (c) phase speed of the most unstable waves as a function of δ and U_o. The reduction in growth rates for small δ is associated with shorter wavelengths and, consequently, the increased role of dissipative terms. The data for the graphs were obtained numerically by solving Eqs. (32) and (33) for $\gamma = 0.003$, $\nu = 0.004$ m^2 s^{-1}, and $\mu = 0.0005$ m^2 s^{-1}.

enological approach to the formulation, which seeks to maintain the essential physics while permitting simplifications of secondary effects. The principal quantitative effect of the drift velocity is on the phase speed of the propagating disturbances. For most of the calculations below we will set $\alpha = 0.2$ and then describe the main effects of changing α.

Since ϕ is a harmonic function, satisfying the Laplace equation, its x and z derivatives at $z = 0$ are related through the Hilbert transform. That is, at $z = 0$

$$\phi_z = \frac{1}{\pi} \mathcal{P} \int_{-\infty}^{\infty} \frac{\phi_x}{x - x'} \, dx', \qquad (39)$$

where $\mathcal{P}$ stands for the Cauchy principal value.

Now introducing

$$\Phi = \phi|_{z=0}, \qquad (40)$$

and rewriting equations (1)–(3) and (36)–(37), with the use of (39), yields a complete system of equations connecting U, h, ζ, η, and Φ:

$$(Uh)_t + (U^2 h)_x + gh\zeta_x = \gamma(U_o^2 - U^2) + \nu(hU_x)_x, \quad (41)$$

$$h_t + (Uh)_x = 0, \qquad (42)$$

$$\zeta = h + \eta - \delta, \qquad (43)$$

$$\eta_t + U_d \eta_x = \frac{1}{\pi} \mathcal{P} \int_{-\infty}^{\infty} \frac{\Phi_x}{x - x'} \, dx' + 2\mu\eta_{xx}, \qquad (44)$$

and

$$\Phi_t + U_d \Phi_x + g\zeta = 2\mu\Phi_{xx}. \qquad (45)$$

We refer to this system as the "quasi nonlinear" approximation since it combines the fully nonlinear equations for the upper layer and linearized equations for the deep layer. In principle, following the derivations of the Benjamin–Ono equation (Benjamin 1967; Ono 1975) in the weakly nonlinear regime, one could derive these equations formally using the characteristic slope of the interface as an expansion parameter.

3. Numerical results: An initial value problem

Equations (41)–(45) are solved numerically, using the explicit Runge–Kutta pair of Bogacki and Shampine (1989) as implemented in Matlab. Second-order finite differencing is used for evaluating the x derivatives and a spectral method for evaluating the Hilbert transform in (44). Periodic boundary conditions are imposed in the x direction. In the numerical experiments the domain of integration ranges from 0.1 to 8 m. The resolution of the numerical scheme is in the range $O(0.1-1$ mm) depending on the wavelength and requirements for numerical stability.

We solve the initial value problem for these equations using as initial conditions the zeroth-order solution described in section 3, that is, a uniform shallow layer with the thickness δ, having a constant velocity U_o, resting on a infinitely deep layer. A spatially varying random perturbation with an $O(0.01$ mm) amplitude is added to the top layer height at time zero. For all calculations we choose $\gamma = 0.003$. With this value of γ, it would take about 10 s to accelerate the top layer from rest to $0.9U_o$. The coefficients of eddy viscosity are $\nu = 0.004$ and $\mu = 0.0005$ m^2 s^{-1}. This choice of damping parameters ensures that the slope of the free surface and the layer interface do not exceed $O(1)$ in regions that correspond to "breaking" or "hydraulic jumps." Smaller viscosity coefficients lead to larger slopes and the possibility of numerical instabilities. Note that an initial value problem with the well-developed upper layer is considered here only for the sake of simplicity. In fact, we ran several experiments where both the depth and the mean velocity of the upper layer could gradually evolve, which led to qualitatively similar results.

Several sets of the calculations are presented. In the first set, the domain of integration extends for only 0.5 m. The results shown in Figs. 5 and 6 suggest that the evolution of the wave field can be divided into three distinct stages. The first is a period of quasi-linear growth that takes place in accordance with the linear stability analysis of section 3. The characteristic length and phase speed of the excited waves (the top row in Fig. 5) approximately coincide with those estimated from Fig. 4. The rapid increase in wave amplitude quickly leads to wave steepening and "breaking" (the very fast rise in the bottom panel in Fig. 6).

It is worth commenting at this point on the representation of breaking in this model. It is clear that realistic breaking, usually associated with wave overturning, intense local mixing, and turbulence at and near the wave crest, is not possible in the model. Effective viscous terms in the equations prevent this from happening. Instead, "breaking" in the model simply implies the formation of strong local gradients of relevant parameters, h_x, U_x, and η_x, which provide the necessary dissipation. This approach has been frequently used for describing wave breaking and front formation (e.g., Fedorov and Melville 1995, 1996, 2000).

Further nonlinear adjustment of the free surface and the interface between the layers lasts for about 15 s (see middle panels in Fig. 5 and the undulating regime of the curves in Fig. 6). Eventually, these processes and dissipation result in the formation of a steady-wave solution propagating in the downwind direction (the bottom panel in Fig. 5). Figure 6 confirms that by time $t = 20$ the wave profile is translating without changing shape at a constant speed.

For the second set of numerical runs (Fig. 7), the domain of integration is extended to 8 m to demonstrate that over intermediate times the characteristic horizontal
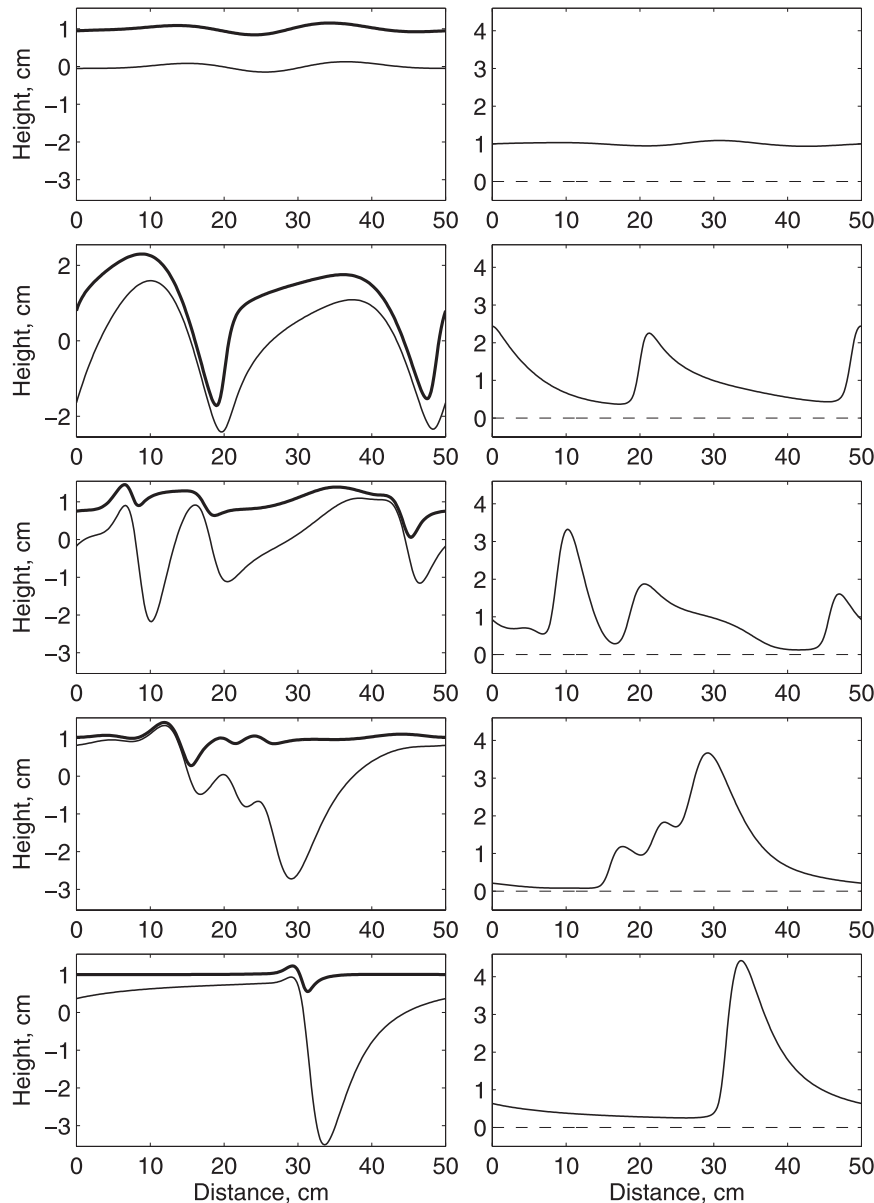
FIG. 5. (left) The elevation of the free surface ζ (the heavy line) and displacement of the layer interface η (the light line) at times $t = 1, 2, 7, 8,$ and 25 s; (right) local thickness h of the upper layer at the same times. The initial conditions correspond to the zeroth-order solution of the system, i.e., a uniform upper layer with a constant velocity, U_o, riding on an infinitely deep layer. A spatially varying random perturbation with an $O(0.01$ mm) amplitude was added to the top-layer thickness at time $t = 0$. The size of the integration domain is 0.5 m. The number of integration points in the x direction is $2^{10} + 1 = 1025$. Note the different stages of wave evolution as described in the text.

scale of the waves is independent of the size of the domain. The wave profile undergoes the same stages of evolution as previously, the main difference being that the solution, even by time $t = 60$, is still evolving, albeit slowly, with the wave profile remaining quasi steady except during overtaking events. The displacement of the interface and the free surface, and the thickness

of the shallow layer, appear as if they are constructed from several steady-wave solutions, each with a slightly different wavelength and amplitude. The characteristic wavelength ($\sim$50 cm in this case) tends to be longer than that of the linear instability for this combination of parameters and increases with time. Similar "reddening," or coarsening, was observed in numerical experiments by
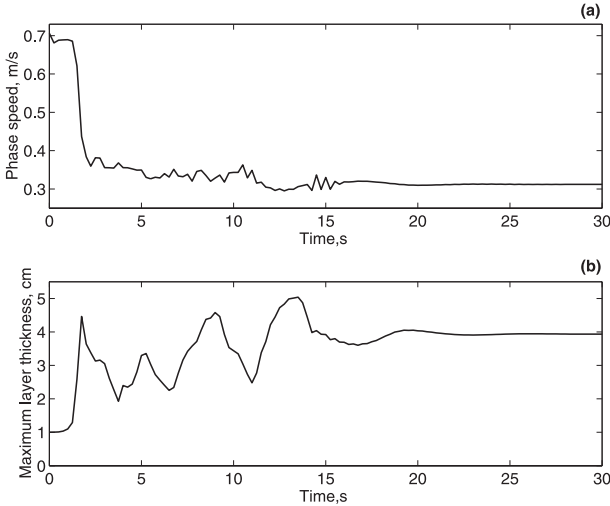
FIG. 6. The characteristic speed of propagating disturbances, calculated as $c = (\langle h_t^2 \rangle / \langle h_x^2 \rangle)^{1/2}$, and maximum thickness of the upper layer as a function of time. After about 20 s of adjustment, the solution is already stationary so that c describes the actual phase speed of the propagating wave. The rapid increase in h and decrease in c, at time $t = 4$ s, is associated with the initial wave steepening and breaking.

Balmforth and Mandre (2004) on the evolution of roll waves. As we show later, this increase in the wavelength is ultimately limited by an instability similar to the original linear instability.

These numerical results suggest that the appearance of the steady or quasi-steady wave solutions is a robust result, and can be expected in domains of arbitrary size. Other calculations over domains of different lengths and with different values of the parameters δ, U_o, U_d, γ, ν, and μ confirm the universal character of this phenomenon. (Note that for small domains we find steady-wave solutions with the wavelength matching the domain size as in Fig. 5. However, for large domains the solution continues to evolve and forms quasi-periodic waves with the characteristic wavelength much shorter than the size of the domain as in Fig. 7.) The next step then is to consider the properties of these solutions in detail.

4. Numerical results: Steady-wave solutions

The structure of the steady-wave solutions is characterized by alternating long intervals, where changes in the streamwise direction occur slowly, and short intervals with rapid changes in the relevant variables (Fig. 8). The displacement of the free surface is small; it is the displacement of the interface between the layers and the thickness of the shallow layer that experience the greatest changes. There is a jump in the thickness of this layer from 0.4 cm to ~4 cm that occurs over a short distance of about 5 cm. This implies a strong local slope, $O(1)$ or even

larger, which we associate with quasi-steady wave breaking. This region of rapid changes in the wave profile, or wave breaking, can be referred to as a hydraulic jump. Before the jump the current is gradually accelerated by the wind, but within the jump the flow is decelerated to lower velocities (Fig. 8c). It is easy to show that the flow is supercritical before (i.e., to the left of the jump) and subcritical after the jump.

That the strongly forced solutions are, indeed, associated with hydraulic jumps can be shown by considering the equations of motion in a flux-conserving or nearly flux-conserving form. After a little algebra, Eqs. (41)–(45) can be written in a steady state as

$$-ch_x + (Uh)_x = 0, \qquad (46)$$

$$-c(Uh)_x + \left(U^2 h + \frac{gh^2}{2} - \frac{g\eta^2}{2} + g\eta\delta - \nu h U_x \right)_x$$
$$= \gamma(U_o^2 - U^2) - g\zeta\eta_x, \qquad (47)$$

and

$$-c\left(\frac{hU^2}{2} + \frac{gh^2}{2} + gh\eta \right)_x$$
$$+ \left(\frac{hU^3}{2} + gUh(h + \eta) - \frac{cg(\eta - \delta)^2}{2} - \nu h U U_x \right)_x$$
$$= \gamma U_o^2 U - \gamma U^3 - cg\zeta\eta_x - \nu h U_x^2, \qquad (48)$$

which reflect mass, momentum, and energy conservation, respectively. [If we set $\eta = 0$, $\nu = 0$, and $\gamma = 0$, the conventional flux-conserving equations in the long-wave approximation are recovered; see Whitham (1974).] Changes in mass, momentum, and energy across the jump are

$$[H]_1^2 = [Uh - ch]_1^2 = 0, \qquad (49)$$

$$[M]_1^2 = \left[U^2 h + \frac{gh^2}{2} - \frac{g\eta^2}{2} + g\eta\delta - \nu h U_x - cUh \right]_1^2 < 0, \qquad (50)$$

and

$$[E]_1^2 = \left[\frac{hU^3}{2} + gUh(h + \eta) - \frac{cg(\eta - \delta)^2}{2} - \nu h U U_x \right.$$
$$\left. - c\left(\frac{hU^2}{2} + \frac{gh^2}{2} + gh\eta \right) \right]_1^2 < 0, \qquad (51)$$
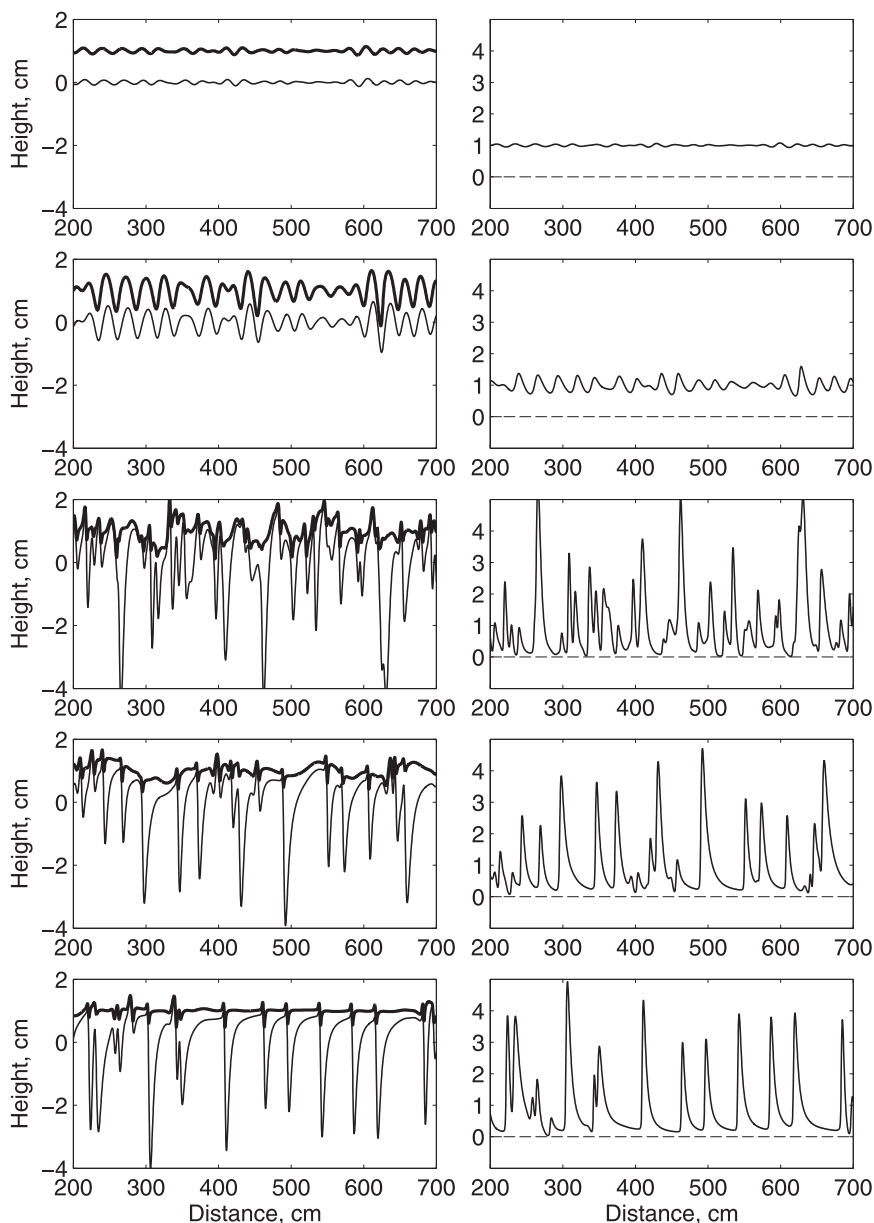
FIG. 7. As in Fig. 5, but the size of the integration domain is now 8 m (of which only 5 m are shown). The number of integration points in the x direction is $2^{13} + 1 = 8193$.

where 1 and 2 refer to points before (i.e., to the left of) the jump and after (i.e., to the right of) the jump, respectively. Mass is conserved across the jump in accordance with (49). Momentum and energy are lost in the jump ($[M]_1^2 < 0$ and $[E]_1^2 < 0$), as seen from Fig. 9 displaying both M and E as a function of x. This differs from classical hydraulic jumps in which only energy is lost while both mass and momentum are conserved.

It is possible to show that these hydraulic jumps are necessary to match the smooth "interior" flow to form a

periodic wave. Since outside the jump variations in the elevation of the free surface ζ and the viscous terms are negligible, in the frame of reference traveling with the wave the equations of motion in the shallow layer reduce to

$$(U - c)U_x = \frac{\gamma(U_o^2 - U^2)}{h},\tag{52}$$

$$[(U - c)h]_x = 0,\tag{53}$$

and
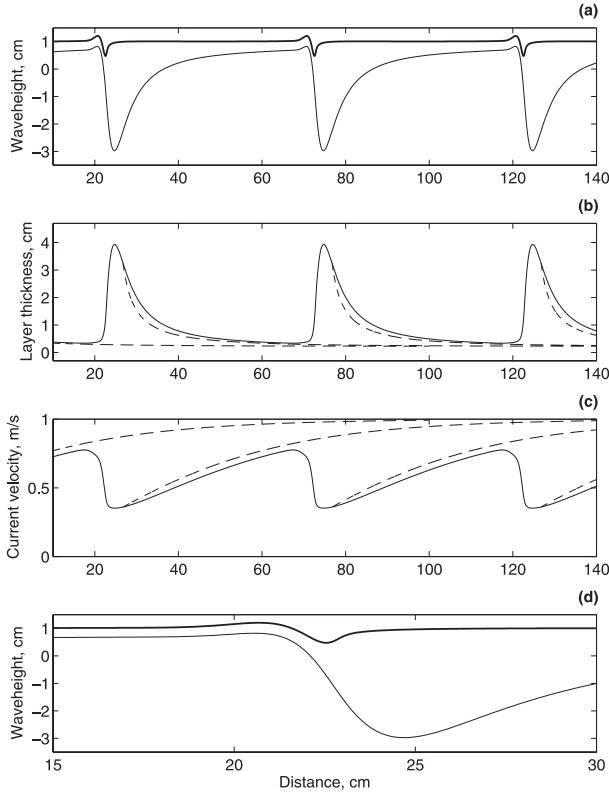
FIG. 8. Details of the steady wave solutions, obtained in the integrations, shown in Fig. 5, with $\mu = 0.0005$ m^2 s^{-1}, $\nu = 0.004$ m^2 s^{-1}, $U_o = 1$ m s^{-1}, $\gamma = 0.003$, $\delta = 1$ cm, and $\lambda = 0.5$ m. The dashed lines show the approximate "interior" solutions to be joined by hydraulic jumps. The waves travel to the right with a constant speed c. (a) The elevation of the free surface ζ (the heavy line) and the displacement of the layer interface η (the light line), (b) the thickness of the upper layer h, (c) the velocity of the flow in the upper layer U, and (d) an expanded version of (a).

$$U|_{x=x_1} = U_1 \quad \text{and} \quad h|_{x=x_1} = h_1, \tag{54}$$

where U_1, h_1 are values of U and h at a reference point x_1. Conditions (54) are added in order to specify a unique solution of the system. Integrating Eqs. (52)–(54) gives

$$U = U_o \tanh[A(x - x_1) + B] \tag{55}$$

and

$$h = h_1 \frac{U_1 - c}{U - c}, \tag{56}$$

where

$$A = \frac{\gamma U_o}{(U_1 - c)h_1}; \quad B = \mathrm{a} \tanh\left(\frac{U_1}{U_o}\right). \tag{57}$$
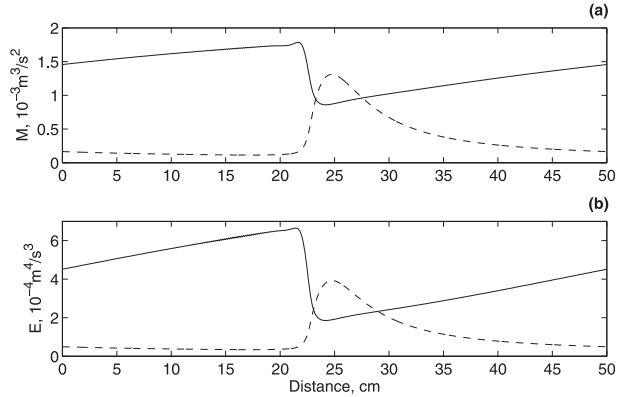

FIG. 9. Momentum and energy fluxes, M and E, as a function of x in the frame of reference moving with the wave to the right. Both energy and momentum are lost in the hydraulic jumps associated with the propagating strongly forced waves. For comparison, the scaled thickness of the upper layer h is shown (the dashed lines): $\mu = 0.0005$ m^2 s^{-1}, $\nu = 0.004$ m^2 s^{-1}, $U_o = 1$ m s^{-1}, $\gamma = 0.003$, $\delta = 1$ cm, and $\lambda = 0.5$ m.

The dashed lines in Fig. 8 exhibit these "interior" solutions to be joined by hydraulic jumps (x_1 is chosen at the point where $h_1 = \delta$). Figures 10 and 11 show strongly forced waves and corresponding interior solutions for other values of λ. [Iteration is used to obtain full solutions for new values of λ. A previous solution is set as the initial condition for Eqs. (41)–(45), and slightly different λ. The model is then run until a new steady state is reached.]

The approximate interior solutions provide a hint of what controls the maximum length of the strongly forced waves. The tangential function in (55) describes a uniform flow for sufficiently large x. According to the analysis of section 3, such flows should be unstable to linear perturbations. The characteristic length beyond which the flow would become uniform is

$$\lambda_{\max} \sim \frac{1}{A} = \frac{(U_1 - c)h_1}{U_o}\frac{1}{\gamma}. \tag{58}$$

Unfortunately, practical use of this estimate is limited because the constant $(U_1 - c)h_1$ is a function of λ (which is not known a priori) and other parameters of the problem. However, one could use it a posteriori to check the results of experiments.

5. The energy and other balances for steady waves

There are several important balances or constraints that control the properties of the strongly forced waves. The most obvious one follows from the equation of mass conservation and implies that the mean thickness of the
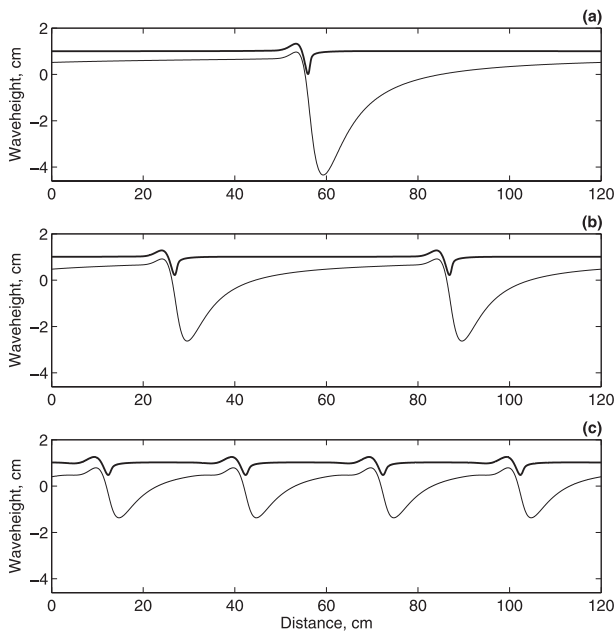
FIG. 10. Steady wave solutions for wavelengths $\lambda = 1.2$, 0.6, and 0.3 m showing elevation of the free surface ζ (the heavy line) and displacement of the layer interface η (the light line): $\mu = 0.0005$ m^2 s^{-1}, $\nu = 0.004$ m^2 s^{-1}, $U_o = 1$ m s^{-1}, $\gamma = 0.003$, and $\delta = 1$ cm.
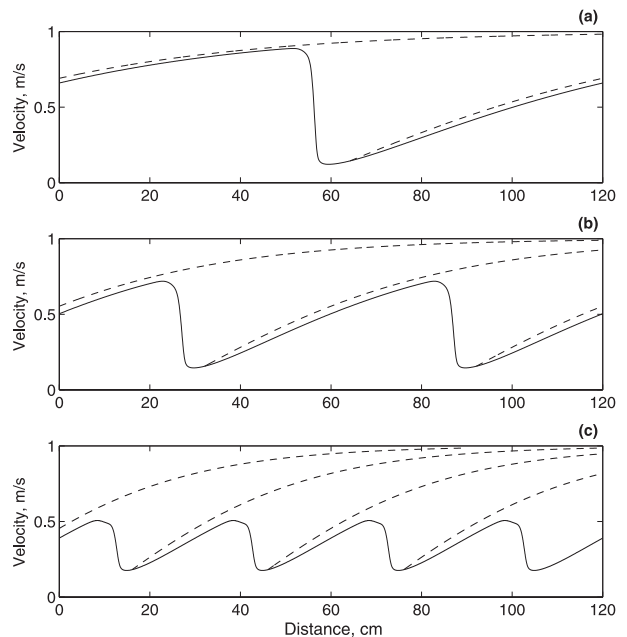

FIG. 11. Steady wave solutions for wavelengths $\lambda = 0.3$, 0.6, and 1.2 m showing the horizontal velocity U in the upper layer for the same conditions as in Fig. 10. The dashed lines show the approximate "interior" solutions to be joined by hydraulic jumps.

upper layer does not change with time; that is, $\overline{h} = \delta$. (Hereafter the bars stand for the average over one wavelength.) The second constraint is dynamical and represents the balance of forces acting on the upper layer. Integrating (41) yields

$$(\overline{Uh})_t + g\overline{h\zeta_x} = \gamma(U_o^2 - \overline{U^2}), \qquad (59)$$

which can be written for the steady state as

$$\gamma U_o^2 = \gamma\overline{U^2} + g\overline{h\eta_x} \qquad (60)$$

or

$$\tau \approx \overline{\tau_i} + \overline{p_i \sin\alpha}, \qquad (61)$$

where

$$p_i = gh \quad \text{and} \quad \sin\alpha \approx \eta_x. \qquad (62)$$

Here τ is the wind stress at the surface, τ_i is the mean interfacial turbulent drag proportional to the square of velocity, and $p_i \sin\alpha$ is the component of hydrostatic pressure tangential to the interface at the bottom of the upper layer. The last term represents a form drag acting at the interface. In the presence of waves, a phase shift between η_x and h causes this term to be nonzero. Thus, the mean current in the upper layer is determined by the

balance between the imposed wind stress and the drag (turbulent plus wave drag) at the interface between the layers.

In the absence of waves, the surface wind stress and the turbulent drag are equal, $\tau = \tau_i$, so that $\overline{U} = U_o$. When waves are present, the magnitude of the wave drag may reach and even exceed the magnitude of the turbulent drag (Fig. 12a). As a result, the average current velocity in the upper layer, $\overline{U}$ (Fig. 12b), may drop significantly lower than U_o but never below the level of the wave phase speed c (Fig. 12c): the strongly forced waves always travel slower than the current.

The reduction of the current velocity in the upper layer can also be explained from the point of view of energy conservation; that is, the surface wind stress does work on the ocean, which is then dissipated by various mechanisms. After a little algebra [see Eqs. (48) and (43)], the energy conservation for the upper layer can be written as

$$\frac{d\overline{\varepsilon}}{dt} = \rho(\gamma U_o^2\overline{U} - \gamma\overline{U^3} - \nu\overline{hU_x^2} + g\overline{h\eta_t}), \qquad (63)$$

where

$$\varepsilon = \frac{\rho}{2}[hU^2 + g(h + \eta)^2 - g\eta^2] = \frac{\rho}{2}(hU^2 + gh^2 + 2gh\eta). \qquad (64)$$
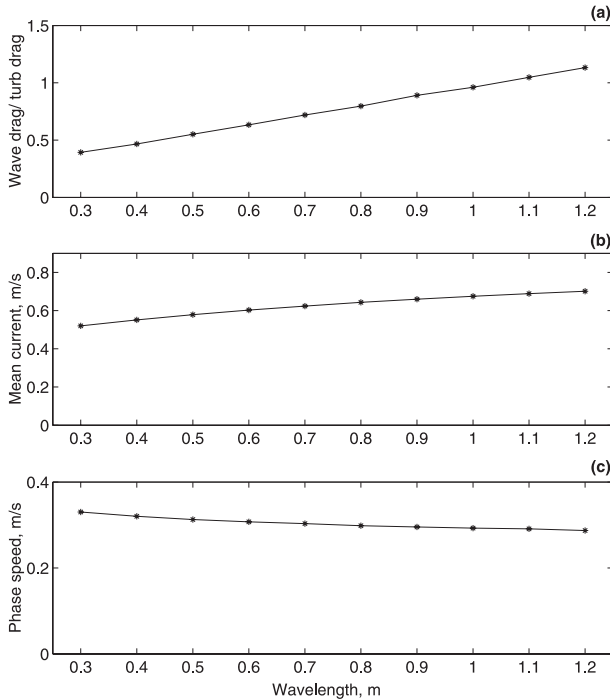
FIG. 12. (a) Ratio of the wave drag, $\overline{gh\eta_x}$, to the turbulent drag, γU^2, both applied at the layer interface and acting on the lower layer; (b) mean speed of the current in the upper layer $\overline{U}$ (m s^{-1}) (note that $\overline{U}$ is smaller than U_o.); and (c) the speed of wave propagation c (m s^{-1})—all as a function of the wavelength: $\mu = 0.0005$ m^2 s^{-1}, $\nu = 0.004$ m^2 s^{-1}, $U_o = 1$ m s^{-1}, $\gamma = 0.003$, $\delta = 1$ cm, and $U_d/U_o = 0.2$.

For the steady state the balance is

$$W + D_{\text{break}} + D_{\text{turb}} + D_{\text{press}} = 0, \tag{65}$$

where

$$W = \rho\gamma U_o^2\overline{U}, \tag{66}$$

$$D_{\text{break}} = -\rho\nu\overline{hU_x^2}, \tag{67}$$

$$D_{\text{turb}} = -\rho\gamma\overline{U^3}, \tag{68}$$

and

$$D_{\text{press}} = +\rho g\overline{h\eta_t}. \tag{69}$$

Here W is the power generated by the surface wind stress working on the mean current in the upper layer (i.e., the rate of work per unit area); D_{break} is the dissipation in the breaking region of the upper layer, and it can be easily shown that the region of breaking with large U_x contributes the most to the integral in (67); D_{turb} is the energy used for the generation of shear and/or

turbulence in the bottom layer by interfacial drag;[3] and D_{press} is the energy needed to perturb the interface between the layers (by hydrostatic pressure), which is then dissipated by the eddy viscosity in the lower layer. Thus, instead of generating surface flow, a significant part of the wind work is transformed into D_{break} and D_{press}.

Various components of the balance in (65) are shown in Fig. 13. Overall, about 20% of the wind work goes directly into wave breaking in the upper layer. This fraction varies from about 5% to 60% for different U_d (see next section). It is important that all the constraints considered in this section do not depend on the approximation used for the lower layer and should remain valid in the fully nonlinear case.

6. The sensitivity of the results to changes in the main parameters

We have conducted a number of calculations exploring the properties of the strongly forced steady waves for different values of the parameters. The iterative approach, similar to that described in section 4, is used again: a gradual change of the chosen parameter in combination with solving equations (41)–(45). The first results concern changes in the steady wave solution when the eddy viscosity μ is modified (Fig. 14). A decrease in μ has a profound effect on the solution. For small μ, the displacement of the layer interface develops a cusp penetrating deep into the water. Then the numerical scheme fails because of an insufficient number of node points to resolve such a singularity. The quasi-nonlinear approximation also fails since nonlinearities become crucial in the lower layer and must be taken into account. Large values of μ effectively make the flow in the lower layer so viscous that the top-layer dynamics become similar to those of a hydraulically controlled flow over bottom topography (Baines 1995).

Changes in the eddy viscosity ν of the upper layer are also important, although to a lesser degree (Fig. 15). With decreasing ν the width of the hydraulic jump is reduced, while the jump in thickness of the shallow layer increases. Below a certain value of ν no steady-state solutions are found, apparently because of small-scale instabilities associated with the sharp corner developed in the wave profile. In effect, the hydraulic jump becomes unable to dissipate a sufficient amount of energy. Overall, we have to use relatively large values of viscosities

---

[3] Although not modeled directly, it is implicitly assumed that the turbulence leads to an enhanced viscosity in the lower layer, which is accounted for in the interfacial boundary conditions. See Eqs. (7) and (8), and Ruvinsky et al. (1991).
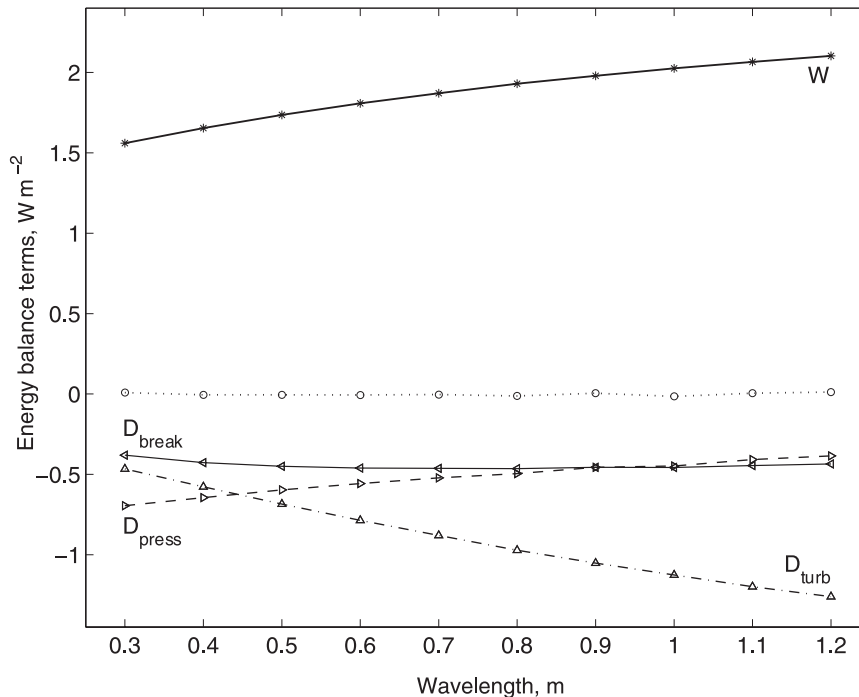
FIG. 13. Different components of the upper-layer energy balance as a function of the wavelength: W, the power generated by the surface wind stress working on the current in the shallow layer (i.e., the rate of work per unit area); D_{break}, energy dissipation in the breaking region of the upper layer; D_{turb}, energy used for the generation of shear and/or turbulence in the bottom layer by the interfacial drag (it is implicitly assumed that this process contributes to an enhanced viscosity in the lower layer); and D_{press}, the energy needed to perturb the interface between the layers (it is eventually dissipated by the eddy viscosity in the lower layer). In the steady state, $W + D_{break} + D_{turb} + D_{press} = 0$. The dotted line shows the sum of the four. For $\mu = 0.0005$ m^2 s^{-1}, $\nu = 0.004$ m^2 s^{-1}, $U_o = 1$ m s^{-1}, $\gamma = 0.003$, $\delta = 1$ cm, and $U_d/U_o = 0.2$.

ν and μ (one to three orders of magnitude larger than regular molecular viscosity) in order to simulate breaking regions with a finite width.

An increase in U_o (Fig. 16) has an effect on the solutions somewhat similar to that of a decrease in ν. A stronger imposed current (i.e., larger U_o) leads to sharper gradients associated with the jump, a smaller width of the jump, and also a stronger surface signature of the waves. Above a certain value of U_o, $O(4$ m s$^{-1})$ for $\lambda = 0.5$ m with the other parameters fixed, no steady-state solutions are found because the slope in the wave profile becomes too steep. For low values of U_o, the solutions lose the character of hydraulic jumps, degenerating into kinematic waves, which completely disappear when $U_o = 0$.

The effects of changes in δ are displayed in Fig. 17. Below and above certain values of δ (about 1 mm and 3 cm, respectively, for $\lambda = 0.5$ m with other parameters fixed), no steady solutions exist, apparently because the "interior" flow becomes unstable. We believe that appropriate values of δ should be of the order of 1–2 cm.

With these numbers the upper-layer thickness can reach 5–10 cm in the breaking region, which appears to be a reasonable number for 50-cm wavelengths.

Finally, variations in γ have a similar effect as changing U_o since increasing (decreasing) γ can increase (reduce) the mean velocity of the current in the upper layer. In addition, in accordance with (58), steady solutions of longer wavelength become attainable for smaller values of γ.

Another important parameter that affects the characteristics of the strongly forced waves is U_d, the mean flow in the lower layer. Because of vertical shear of the horizontal velocities, one can expect a transfer of momentum from the upper layer to the lower layer, inducing an accelerating current there. We have parameterized the speed of this current as $U_d = \alpha U_o (0 < \alpha < 1)$. The momentum transfer is a time-dependent process so that fixing α as a constant is valid only for shorter time scales. Particular values of α do not change the wave profile qualitatively; however, they do influence the phase speed of the solution in the laboratory
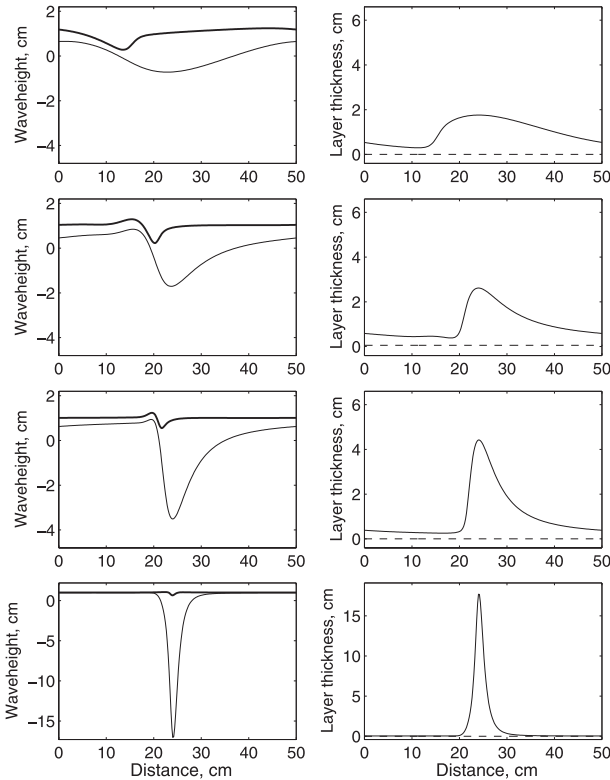
FIG. 14. Steady wave solutions for different values of the eddy viscosity, μ, of the lower layer for $\nu = 0.004$ m^2 s^{-1}, $U_o = 1$ m s^{-1}; $\gamma = 0.003$, $\delta = 1$ cm, and $\lambda = 0.5$ m: elevation of the free surface, ζ (the heavy line) and displacement of the layer interface, η (the light line). From top to bottom: $\mu = 1000, 200, 50$, and 1×10^{-5} m^2 s^{-1}. Corresponding values of the phase velocity obtained from our calculations are $c = 0.65, 0.47, 0.32$, and 0.24 m s^{-1}. Note that at very high values of μ, the flow in the lower layer is effectively so viscous that the solution in the upper layer effectively resembles a jump in a hydraulically controlled flow over the bottom topography. At low values of μ, the interface develops a singularity, and the quasi-non-linear approximation fails.

FIG. 15. Steady wave solutions for different values of the eddy viscosity ν of the upper layer for $\mu = 0.0005$ m^2 s^{-1}, $U_o = 1$ m s^{-1}, $\gamma = 0.003$, $\delta = 1$ cm, and $\lambda = 0.5$ m: elevation of the free-surface ζ (the heavy line) and of the displacement of the layer interface η (the light line). From top to bottom $\nu = 20, 4$, and 1 ($\times 10^{-3}$ m^2 s^{-1}). Corresponding values of the phase velocity, as obtained from calculations, are $c = 0.45, 0.32$, and 0.30 m s^{-1}.

frame of reference, and the amount of energy lost in the wave breaking. The phase speed increases almost linearly with U_d, while the relative loss of energy in the breaking region drops sharply for large U_d (Fig. 18). The most appropriate values of α for this model should lie in the range 0.1–0.4 (0.2 was used in most of the calculations.)

In summary, changes in different parameters affect both the "interior" flow and the local properties of the jump, making steady wave solutions possible in a broad parameter range of different combinations of wavelength λ and parameters μ, ν, δ, γ, U_d, and U_o. It is noteworthy that an increase in μ, ν, U_d, or U_o and a reduction in δ increase the thickness of the jump in the x direction and result in a larger phase speed of the waves. A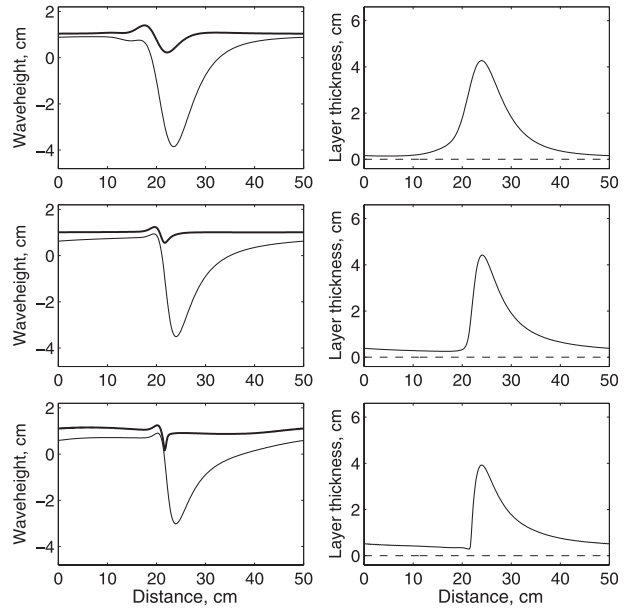lso note that some of the solutions, especially at larger values of λ or δ, can become unstable due to slow modulational instabilities.

7. Discussion and conclusions

We have shown that there exist strongly forced surface waves in a two-layer fluid that consists of a shallow wind-driven turbulent layer on the surface of an infinitely deep fluid. These waves propagate in the downwind direction, significantly modifying the flow in both layers. The wave structure is characterized by long intervals where the current is gradually accelerated by the wind, separated by relatively short confined regions associated with quasi-steady wave breaking where the flow is decelerated to lower velocities. The regions of breaking (described in our model as regions of strong gradients in the relevant parameters) can be referred to as hydraulic jumps that are necessary to match the smooth "interior" flow in a periodic wave train.

The mean current in the upper layer is determined by the balance between the surface wind stress and the drag at the interface between the layers. This interfacial drag has two components: turbulent drag modeled as proportional to the second power of the current velocity and wave drag, whose magnitude may actually exceed that of the former. (In the absence of the waves, the surface
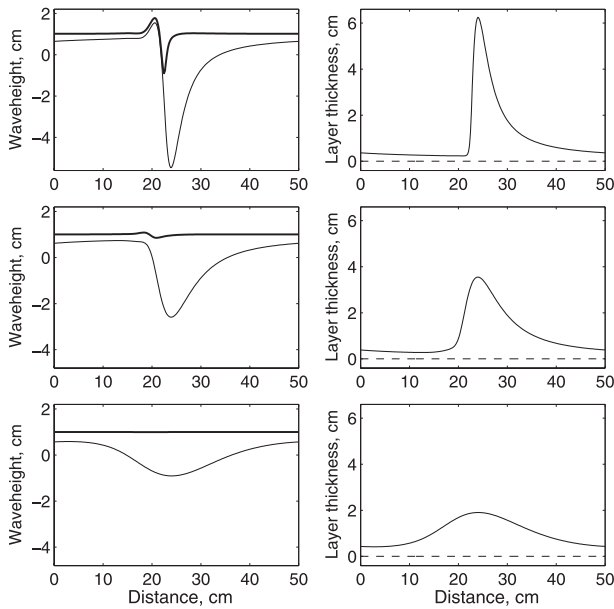
FIG. 16. Steady wave solutions for different values of U_o for $\mu = 0.0005 \text{ m}^2 \text{ s}^{-1}$, $\nu = 0.004 \text{ m}^2 \text{ s}^{-1}$, $\delta = 1 \text{ cm}$, $\gamma = 0.003$, and $\lambda = 0.5 \text{ m}$: elevation of the free-surface ζ (the heavy line) and of the displacement of the layer interface η (the light line). From top to bottom $U_o = 2.5$, 0.5, and 0.05 m s^{-1}; corresponding values of the phase velocity are $c = 0.37$, 0.30, and 0.25 m s^{-1}.

FIG. 17. Steady wave solutions for different values of δ for $\mu = 0.0005 \text{ m}^2 \text{ s}^{-1}$, $\nu = 0.004 \text{ m}^2 \text{ s}^{-1}$, $U_o = 1 \text{ m s}^{-1}$, $\gamma = 0.003$, and $\lambda = 0.5 \text{ m}$: elevation of the free-surface ζ (the heavy line) and the displacement of the layer interface η (the light line). From top to bottom, $\delta = 1.8$, 0.5, and 0.2 cm. Corresponding values of the phase velocity $c = 0.30$, 0.38, and 0.50 m s^{-1}.

wind stress and the turbulent drag balance each other.) The wind stress does work on the ocean, which is then dissipated through three main mechanisms: 1) dissipation in the breaking region, 2) the work of the hydrostatic pressure needed to perturb the interface between the layers (it is eventually dissipated by the eddy viscosity in the lower layer), and 3) the generation of shear or turbulence in the bottom layer by the interfacial stress. (Although not modeled directly, it is implicitly assumed that this mechanism leads to an enhanced viscosity in the lower layer.)

It is tempting to compare these strongly forced solutions to the roll waves in shallow water on an inclined plane, but there are important differences. Unlike classical hydraulic jumps (as discussed in Lighthill 1978), the strongly forced solutions lose not only energy across the jump but momentum as well. To that end, these jumps must have a finite thickness in the x direction. These and other differences make a direct comparison with roll waves somewhat limited. The roll waves are basically long nonlinear gravity waves and, as such, travel with a speed faster then that of the mean current. In contrast, the strongly forced wave solutions propagate with speeds smaller than the mean current of the upper layer. (One can easily observe this in the wave field generated by the downwash of a low-flying helicopter, if the trajectories of air bubbles that act as passive tracers are followed.
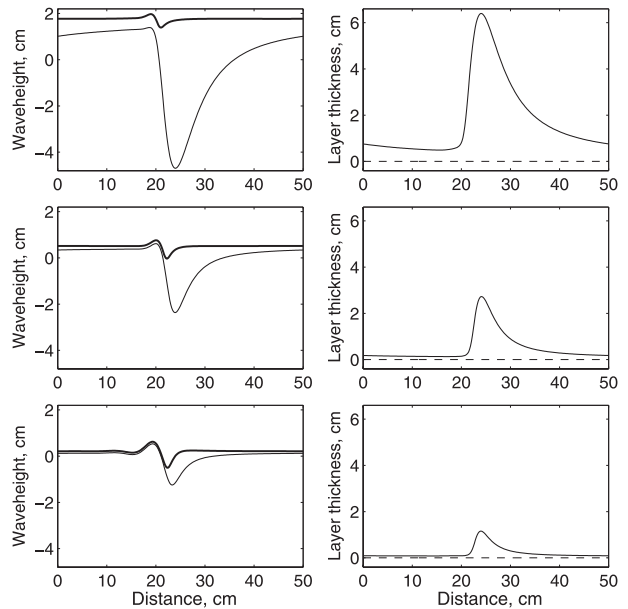
Within the frame of reference traveling with the waves, the bubbles quickly move toward the region of breaking where their trajectory is pushed downward with a considerable acceleration.) If one uses the frame of reference traveling with the waves in both cases, that is, for the classical roll waves and the strongly forced wind waves described here, this difference disappears.

One of the important effects of the strongly forced waves, besides generating enhanced turbulence by wave breaking, is to reduce the mean speed of the surface current in the upper layer, as compared to the case of a uniform wind-driven layer. The speed of the current can decrease by a factor of 2–5, depending on the wavelength, eddy viscosity, and other parameters. In effect, the wind work goes directly into wave breaking and turbulence.

The evolution of an initially undisturbed wind-driven layer follows a simple scenario: linear instability leads to wave growth and steepening and, eventually, breaking. Further adjustment results in the formation of quasi-steady wave solutions. Continual interactions among those (with wave breaking and also with the excitation of free surface waves) lead to the establishment of a characteristic wavelength, which is usually longer than that of the linear instability. This wavelength has a tendency to grow; however, it is limited by an instability, similar to the original linear instability, that tends to
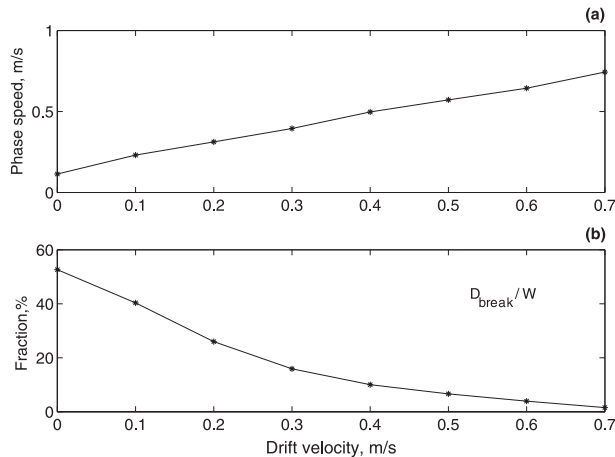
FIG. 18. The wave phase speed, c, and the ratio D_{break}/W as a function of the drift velocity, U_d, in the lower layer, for $\mu = 0.0005 \text{ m}^2 \text{ s}^{-1}$, $\nu = 0.004 \text{ m}^2 \text{ s}^{-1}$, $U_o = 1 \text{ m s}^{-1}$, $\gamma = 0.003$, $\delta = 1$ cm, and $\lambda = 0.5$ m.

develop on smooth parts of the wave profile as the wavelength becomes too long.

Under less strongly forced conditions, intermittent microscale wave breaking in which there is no significant air entrainment has been recognized at least since the work of Banner and Phillips (1974). Such breaking may result from the instability of parasitic capillary waves generated on the forward faces of short gravity–capillary waves (Duncan et al. 1994, 1999; Duncan and Dimas 1999; Fedorov et al. 1998; Jiang et al. 1999; Perlin and Schultz 2000). Even in the absence of breaking, it has been shown that parasitic capillaries may lead to significantly enhanced radiation damping of longer gravity–capillary waves (Ruvinsky et al. 1991; Longuet-Higgins 1995; Fedorov and Melville 1998). Kolmogorov-type weak turbulence theories of wind wave generation and evolution (Zakharov et al. 1992) would have essentially all of the dissipation occurring in these short unresolved waves while the dynamics of the longer resolved waves are the result of wind forcing and weakly nonlinear wave–wave interactions. A more complete model of strongly forced waves would need to include these effects of surface tension and surface curvature and, perhaps, flow separation near the crests of these steep short waves (Longuet-Higgins 1990).

The above description reveals several limitations of our model. The first is that the wave breaking is numerical, as there is no wave overturning possible in the system. The second is that the upper-layer thickness and the coefficients of eddy viscosity are assumed to be fixed. In reality, one would expect a gradual deepening of the top layer, accompanied by changes in the turbulence and mixing. Last, but not least, are the limitations imposed

by the quasi-nonlinear approximation. While making the problem more tractable, it also defines its main weaknesses. From Figs. 5 and 7, or Figs. 14 and 15, it is clear that unless relatively high values of eddy viscosity are used, the slope of the interface may exceed $O(1)$, implying that a fully nonlinear approach is desirable. The model also assumes a relatively simple (constant stress) forcing by the wind, whereas the flow in the air and water are coupled so that the evolution of the surface layer and surface waves feed back onto the airflow. It is most unlikely that significant progress can be made in this area without resorting to direct numerical simulation (DNS) or large eddy simulation (LES) of strongly nonlinear (e.g., Iafrati and Campana 2003) and coupled flows.

Despite these limitations, the results are surprisingly robust in a very broad range of parameters. We were able to reproduce the strongly forced solutions in the range of wavelengths from 10 cm to 4 m, using eddy viscosities of the upper layer in the range $O(10^{-3}–10^{-2} \text{ m}^2 \text{ s}^{-1})$, eddy viscosities of the lower layer in the range $O(10^{-5}–10^{-2} \text{ m}^2 \text{ s}^{-1})$, and different values of U_o, U_d, γ, and δ. We have investigated how the effect of variations in normal pressure related to variations in surface slope influence our solutions; see appendix A. (These are variations in normal pressure that induce form drag.) We find that over a broad range of parameters, reflecting the relative importance of the form drag, the structure and qualitative behavior of the solutions remain unchanged. Furthermore, the model results show qualitative agreement with the two examples presented in Fig. 1: the waves "break" continuously at each crest, and the wave phase speed is slower than the surface flow (for the helicopter downwash). This suggests that developments of the model may be applicable in describing strongly forced surface wave fields. However, such developments should be pursued in concert with experiments to test the essential ideas of the model. For example, rapid distortion theory, or even empirical data on the parameterization of turbulence in accelerating flows, might be used to relax the assumption of constant eddy viscosities,[4] but this should be done in concert with measurements of the turbulent properties of the surface layer, and the dispersion relationship for strongly forced surface waves. As far as we are aware, there are no empirical data with which to compare this model.

---

[4] A simple model with viscosity in the upper layer depending on the horizontal gradient of the layer thickness is discussed in appendix B.

APPENDIX A

The Role of Normal Surface Pressure

In the main body of the text we assumed that the dominant effect of winds on the ocean is in generating surface flow in the upper layer via tangential wind stress. To evaluate the effect of normal pressure generated by the airflow above a wavy surface, we now add to the momentum equations (41) and (45) a simple parameterization of normal pressure anomalies, which allows for a surface form drag:

$$(Uh)_t + (U^2 h)_x + h(P/\rho)_x = \gamma(U_o^2 - U^2) - \nu(hU_x)_x, \quad \text{(A1)}$$

$$\Phi_t + U_d \Phi_x + (P/\rho) = 2\mu \Phi_{xx}, \quad \text{(A2)}$$

with

$$P/\rho = g(\zeta + L_p \zeta_x). \quad \text{(A3)}$$

Here P includes the hydrostatic component associated with the modulation of the height of the free surface ($\rho g \zeta$) as used in the body of the paper along with an additional term ($\rho g L_p \zeta_x$) that is in phase with the surface slope. This latter term leads to a form drag and hence wave growth.

The characteristic length, L_p, is introduced to describe the relative magnitude of the form drag. In general, L_p is a function of the wind speed and the surface wavelength. If one uses (A3) in the conventional theory of irrotational linear surface gravity waves (e.g., Whitham 1974), the calculated amplitude growth rate Γ for a monochromatic wave is given by

$$\Gamma = \frac{ck^2 L_p}{2} = \frac{2\pi^2 cL_p}{\lambda^2} = \pi L_p \left(\frac{2\pi g}{\lambda^3}\right)^{1/2}. \quad \text{(A4)}$$

For surface gravity waves with $\lambda = 0.5$ m and $L_p = 0.005$ m, this expression gives $\Gamma = 0.35$ s^{-1}, or roughly 3 s as the *e*-folding time scale for wave growth, which can be
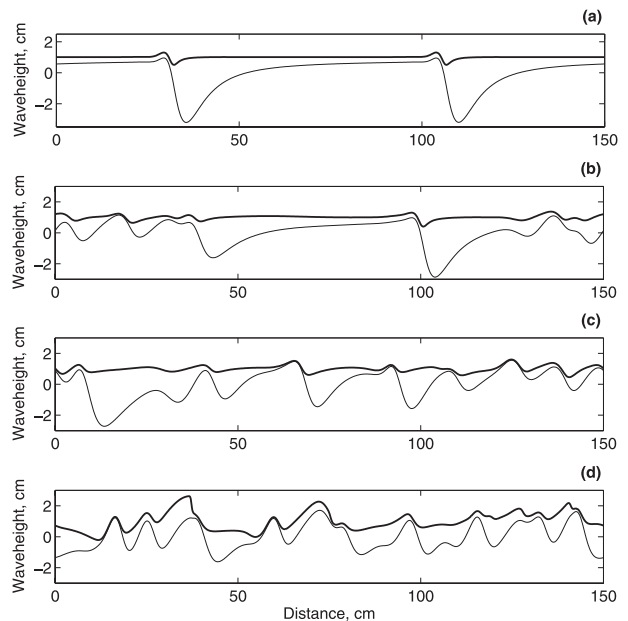

FIG. A1. Elevation of the free-surface ζ (heavy line) and displacement of the layer interface η (light line) for $\mu = 0.0005$ m^2 s^{-1}, $\nu = 0.004$ m^2 s^{-1}, $U_o = 1$ m s^{-1}, $\gamma = 0.003$, and $\delta = 1$ cm: (a) a steady wave solution for $L_p = 0.003$ m and $\lambda = 0.75$ m; (b)–(d): typical quasi-periodic time-dependent solutions for $L_p = 0.003$ m, 0.006 m, and 0.01 m.

achieved only at high wind speeds (see Komen et al. 1994, p. 85, Fig. 2.3).

We have conducted multiple numerical experiments to investigate the properties of the solutions with the modifications given in Eqs. (A1)–(A3) and the results are as follows (Fig. A1). For values of L_p smaller than approximately 0.005 m both steady waves and quasiperiodic solutions exist, very similar to the ones described in the main body of the paper. The limit 0.005 m depends to some extent on the parameters used for the calculations, including ν, μ, and λ.

For values of L_p larger than 0.005 m, steady wave solutions become unstable almost immediately, but the solutions still represent quasiperiodic strongly forced waves with regions of strong breaking. One of the effects of surface pressure variations simulated by our simple model is to add short-wave undulations that reduce the typical wavelength of the solutions (Fig. A1c). Another effect is to increase the surface height of the waves and, at the same time, to introduce irregular long-wave modulations of the solutions.

Finally, for values of L_p approaching or larger than 0.01 m, the waves become more and more chaotic and resemble our original solutions less and less. Nevertheless, one can still recognize the regions of wave breaking characterized by steep gradients on the forward face of the waves (Fig. A1d). Based on these results, it appears

likely that different balances of the total surface stress between shear and normal stresses may lead to different strongly forced wave regimes.

APPENDIX B

Varying Eddy Viscosity in the Upper Layer

In the main body of the paper, we used constant values of eddy viscosity for the upper layer. However, it is clear that wave breaking occurs only in confined areas, which we expect will have narrow regions of elevated viscosity. To take this effect into account, one can parameterize viscosity as a function of the upper-layer thickness, for example see Fig. B1.

We have tried several such parameterizations, all of which work quite well with an appropriate choice of parameters. For the sake of brevity, in this appendix we describe only one such representation:

$$\nu = \nu_0 \left[0.1 + 0.9 \left(\frac{\partial h}{\partial x} \right)^2 \right]. \tag{B1}$$

Here viscosity ν is proportional to a base value ν_0 multiplied by a factor, varying along the wave as a function of the horizontal gradient in the thickness of the upper layer. The numerical coefficients in (B1) could be easily changed, but that would lead only to minor modifications in the wave profiles.

The difference between solutions with constant and varying viscosities is rather small (Fig. B1a), even though
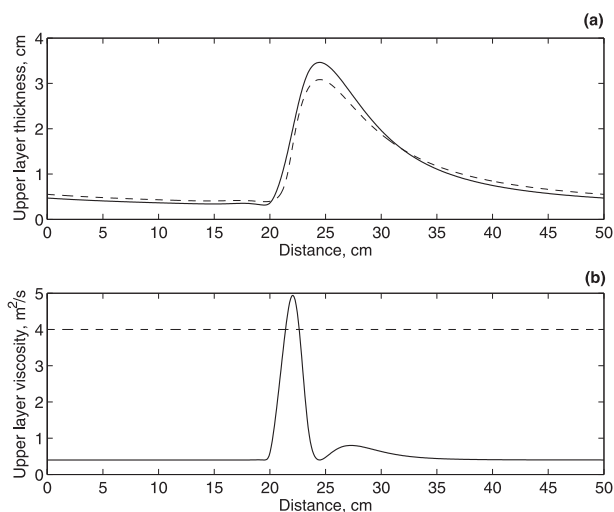

FIG. B1. (a) Thickness of the upper layer h for a steady wave solution ($\lambda = 0.5$ m) with varying viscosity ν (solid line) and constant viscosity ν_0 (dashed line) for $\mu = 0.0005$ m^2 s^{-1}, $U_o = 1$ m s^{-1}, $\gamma = 0.003$, and $\delta = 1$ cm; (b) corresponding values of viscosities ν and ν_0.

viscosity along the wave profile in the latter case (except in the breaking region) is an order of magnitude smaller than the value originally used.

REFERENCES

Baines, P. G., 1995: *Topographic Effects in Stratified Flows*. Cambridge University Press, 482 pp.

Balmforth, N. J., and S. Mandre, 2004: Dynamics of roll waves. *J. Fluid Mech.,* **514,** 1–33.

Banner, M. L., and O. M. Phillips, 1974: On the incipient breaking of small-scale waves. *J. Fluid Mech.,* **65,** 647–656.

——, and W. K. Melville, 1976: On the separation of airflow over water waves. *J. Fluid Mech.,* **77,** 825–842.

Benjamin, T. B., 1967: Internal waves of permanent form in fluids of great depth. *J. Fluid Mech.,* **29,** 559–562.

Bogacki, P., and L. F. Shampine, 1989: A 3(2) pair of Runge–Kutta formulas. *Appl. Math. Lett.,* **2,** 1–9.

Dommermuth, D. G., 1994: Efficient simulation of short and long-wave interactions with applications to capillary waves. *Trans. ASME: J. Fluids Eng.,* **116,** 77–82.

Donelan, M. A., B. K. Haus, N. Reul, W. J. Plant, M. Stiassnie, H. C. Graber, O. B. Brown, and E. S. Saltzman, 2004: On the limiting aerodynamic roughness of the ocean in very strong winds. *Geophys. Res. Lett.,* **31,** L18306, doi:10.1029/2004GL019460.

Dressler, R. F., 1949: Mathematical solution of the problem of roll waves in inclined open channels. *Commun. Pure Appl. Math.,* **2,** 149–194.

Duncan, J. H., and A. A. Dimas, 1999: Surface ripples due to steady breaking waves. *J. Fluid Mech.,* **329,** 309–339.

——, V. Philomin, M. Behres, and J. Kimmel, 1994: The formation of spilling breaking water waves. *Phys. Fluids,* **6,** 2558–2560.

——, H. Qiao, V. Philomin, and A. Wenz, 1999: Gentle spilling breakers: Crest profile evolution. *J. Fluid Mech.,* **379,** 191–222.

Fedorov, A. V., and W. K. Melville, 1995: Propagation and breaking of nonlinear Kelvin waves. *J. Phys. Oceanogr.,* **25,** 2519–2531.

——, and ——, 1996: Hydraulic jumps at boundaries in rotating fluids. *J. Fluid Mech.,* **324,** 55–82.

——, and ——, 1998: Nonlinear gravity-capillary waves with forcing and dissipation. *J. Fluid Mech.,* **354,** 1–42.

——, and ——, 2000: Kelvin fronts on the equatorial thermocline. *J. Phys. Oceanogr.,* **30,** 1692–1705.

——, ——, and A. Rozenberg, 1998: Experimental and numerical study of parasitic capillary waves. *Phys. Fluids,* **10,** 1315–1323.

Gent, P. R., 1993: The energetically consistent shallow water equations. *J. Atmos. Sci.,* **50,** 1323–1325.

Iafrati, A., and E. F. Campana, 2003: A domain decomposition approach to compute wave breaking (wave-breaking flows). *Int. J. Numer. Methods Fluids,* **41,** 419–445.

Jiang, L., H. J. Lin, W. W. Schultz, and M. Perlin, 1999: Unsteady ripple generation on steep gravity-capillary waves. *J. Fluid Mech.,* **386,** 281–304.

Komen, G. K., L. Cavaleri, M. Donelan, K. Hasselmann, S. Hasselmann, and P. A. E. M. Janssen, 1994: *Dynamics and Modelling of Ocean Waves*. Cambridge University Press, 532 pp.

Lighthill, M. J., 1978: *Waves in Fluids*. Cambridge University Press, 504 pp.

Longuet-Higgins, M. S., 1990: Flow separation near the crests of short gravity waves. *J. Phys. Oceanogr.,* **20,** 595–599.

——, 1992: Theory of weakly damped Stokes waves: A new formulation and a physical interpretation. *J. Fluid Mech.,* **235,** 319–324.

——, 1995: Parasitic capillary waves: A direct calculation. *J. Fluid Mech.,* **301,** 79–107.

——, 1998: Instabilities of a horizontal shear flow with a free surface. *J. Fluid Mech.,* **364,** 147–162.

Melville, W. K., 1996: The role of surface-wave breaking in air–sea interaction. *Annu. Rev. Fluid Mech.,* **28,** 279–321.

Miles, J. W., 1957: On the generation of surface waves by shear flows. Part 1. *J. Fluid Mech.,* **3,** 185–204.

——, 1959: On the generation of surface waves by shear flows. Part 2. *J. Fluid Mech.,* **6,** 568–582.

Milinazzo, F. A., and P. G. Saffman, 1990: Effect of a surface shear layer on gravity and gravity-capillary waves of permanent form. *J. Fluid Mech.,* **216,** 93–101.

Morland, L. C., P. G. Saffman, and H. C. Yuen, 1991: Waves generated by shear layer instabilities. *Proc. Roy. Soc. London,* **433A,** 441–450.

Ng, C. O., and C. C. Mei, 1994: Roll waves on a shallow layer of mud modelled as a power-law fluid. *J. Fluid Mech.,* **263,** 151–183.

Ono, H., 1975: Algebraic solitary waves in stratified fluids. *J. Phys. Soc. Japan,* **39,** 1082–1091.

Perlin, M., and W. W. Schultz, 2000: Capillary effects on surface waves. *Annu. Rev. Fluid Mech.,* **32,** 241–274.

Powell, M. D., P. J. Vickery, and T. A. Reinhold, 2003: Reduced drag coefficient for high wind speeds in tropical cyclones. *Nature,* **422,** 279–283.

Ruvinsky, K. D., F. I. Feldstein, and G. I. Freidman, 1991: Numerical simulations of the quasi-stationary stage of ripple excitation by steep gravity-capillary waves. *J. Fluid Mech.,* **230,** 339–353.

Shrira, V. I., 1993: Surface waves on shear currents: Solution of the boundary-value problem. *J. Fluid Mech.,* **252,** 565–584.

Whitham, G. B., 1974: *Linear and Nonlinear Waves.* John Wiley and Sons, 636 pp.

Zakharov, V. E., V. S. L'vov, and G. Falkovich, 1992: *Kolmogorov Spectra of Turbulence I: Wave Turbulence.* Springer-Verlag, 264 pp.